Discovery of *N*-(4-{[5-Fluoro-7-(2-methoxyethoxy)quinazolin-4-yl]amino}phenyl)-2-[4-(propan-2-yl)-1*H*-1,2,3-triazol-1-yl]acetamide (AZD3229), a Potent Pan-KIT Mutant Inhibitor for the Treatment of Gastrointestinal Stromal Tumors

Jason G. Kettle,*[†] Rana Anjum,[§] Evan Barry,[§,⊥] Deepa Bhavsar,[§] Crystal Brown,[§] Scott Boyd,[†] Andrew Campbell,[†] Kristin Goldberg,[†] Michael Grondine,[§] Sylvie Guichard,[§,#] Christopher J. Hardy,[‡] Tom Hunt,[†] Rhys D. O. Jones,[†] Xiuwei Li,[∥] Olga Moleva,[†] Derek Ogg,[‡,∇] Ross C. Overman,[‡] Martin J. Packer,[†] Stuart Pearson,[†] Marianne Schimpl,[‡] Wenlin Shao,[§] Aaron Smith,[†] James M. Smith,[†] Darren Stead,[†] Steve Stokes,[†] Michael Tucker,[†] and Yang Ye[∥]

[†]Oncology, IMED Biotech Unit, AstraZeneca, Unit 310, Darwin Building, Cambridge Science Park, Milton Road, Cambridge CB4 0WG, United Kingdom

[‡]Discovery Sciences, IMED Biotech Unit, AstraZeneca, Unit 310, Darwin Building, Cambridge Science Park, Milton Road, Cambridge CB4 0WG, United Kingdom

[§]Oncology, IMED Biotech Unit, AstraZeneca, 35 Gatehouse Park, Waltham, Massachusetts 02451, United States

[∥]Pharmaron Beijing Co., Ltd., 6 Taihe Road BDA, Beijing 100176, P. R. China

S *Supporting Information*

AZD3229 bound to c-KIT
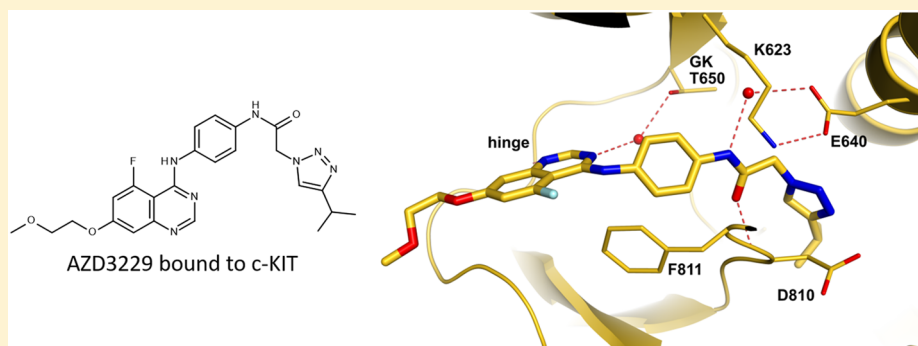
ABSTRACT: While the treatment of gastrointestinal stromal tumors (GISTs) has been revolutionized by the application of targeted tyrosine kinase inhibitors capable of inhibiting KIT-driven proliferation, diverse mutations to this kinase drive resistance to established therapies. Here we describe the identification of potent pan-KIT mutant kinase inhibitors that can be dosed without being limited by the tolerability issues seen with multitargeted agents. This effort focused on identification and optimization of an existing kinase scaffold through the use of structure-based design. Starting from a series of previously reported phenoxyquinazoline and quinoline based inhibitors of the tyrosine kinase PDGFRα, potency against a diverse panel of mutant KIT driven Ba/F3 cell lines was optimized, with a particular focus on reducing activity against a KDR driven cell model in order to limit the potential for hypertension commonly seen in second and third line GIST therapies. AZD3229 demonstrates potent single digit nM growth inhibition across a broad cell panel, with good margin to KDR-driven effects. Selectivity over KDR can be rationalized predominantly by the interaction of water molecules with the protein and ligand in the active site, and its kinome selectivity is similar to the best of the approved GIST agents. This compound demonstrates excellent cross-species pharmacokinetics, shows strong pharmacodynamic inhibition of target, and is active in several in vivo models of GIST.

■ INTRODUCTION

Gastrointestinal stromal tumors (GISTs) are soft tissue sarcomas of the gastrointestinal (GI) tract that are driven predominantly through aberrant signaling of the proto-oncogene c-KIT.[1] Following surgical resection, 5-year survival rates vary from 35−65% depending on the size of tumor, mitotic potential, and where it is located.[2] While incidence is relatively rare, estimated to be of the order of 1.5 patients per 100 000 population annually[3] (annual incidence in the United States is
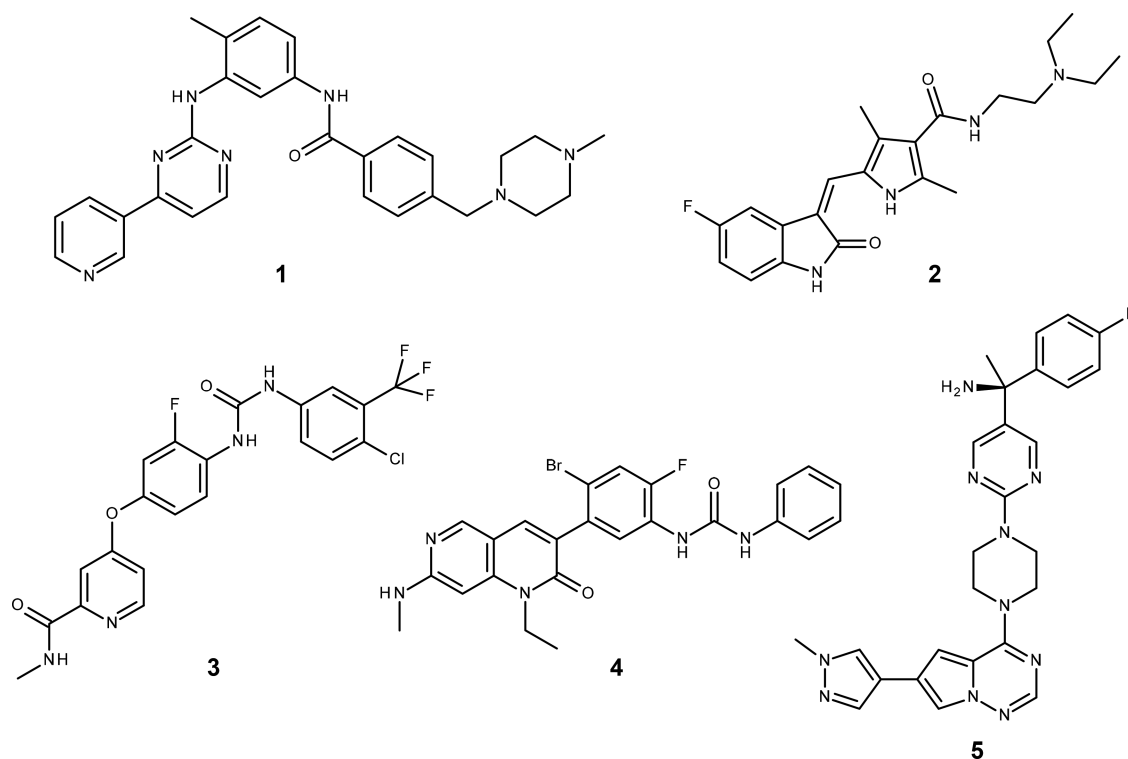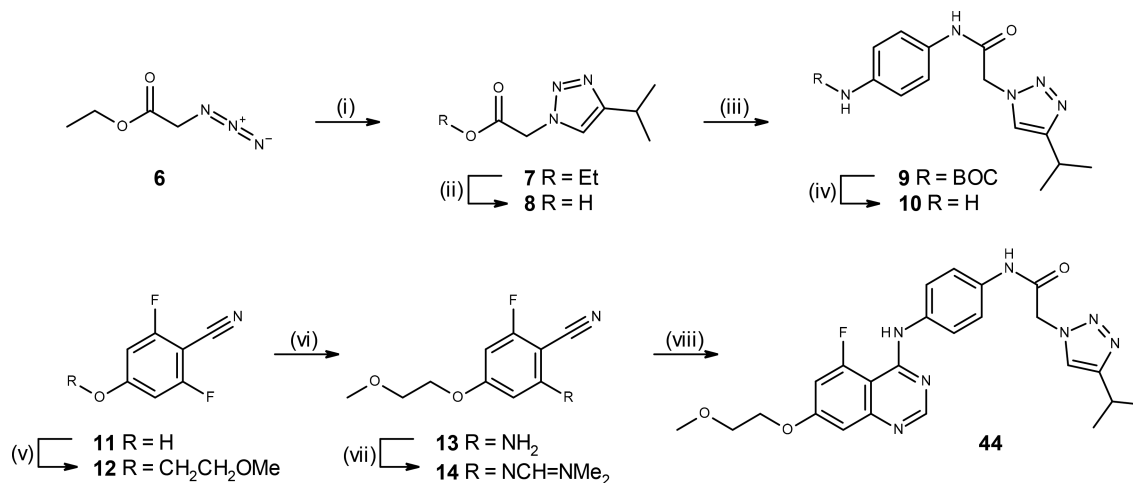
Figure 1. Approved GIST therapies and agents in clinical trials. Imatinib **1**, sunitinib **2**, and regorafenib **3** are approved as first, second, and third line treatments, respectively. Ripretinib (DCC-2618) **4** and avapritinib (BLU-285) **5** are currently undergoing clinical trials in GIST patients.

Scheme 1. Synthesis of Compound 44[a]

[a]Reagents and conditions: (i) CuI, 3-methylbut-1-yne, Et$_3$N, CH$_3$CN, 20 °C, 3 days, 90%; (ii) LiOH, water, THF, 20 °C, 1.5 h, 100%; (iii) *tert*-butyl *N*-(4-aminophenyl)carbamate, HATU, DIPEA, DMF, 20 °C, 16 h, 57%; (iv) 4 M HCl in dioxane, MeOH, DCM, 20 °C, 3 h, 89%; (v) 1-bromo-2-methoxyethane, K$_2$CO$_3$, DMF, 85 °C, 5 h, 93%; (vi) aq NH$_3$, *i*-PrOH, 100 °C, 13 h, 87%; (vii) 1,1-dimethoxy-*N*,*N*-dimethylmethanamine, 80 °C, 2 h, 100%; (viii) **10**, acetic acid, 60 °C, 35 min, 58%.

estimated at 3800),[4] GIST is still the most common mesenchymal tumor of the GI tract, with the majority harboring activating mutations of this receptor tyrosine kinase.[5] Such mutations are diverse and heterogeneous, spanning the kinase domain of KIT with single point amino acid transpositions in the ATP binding pocket, sequence deletions in exon 11, insertions in exon 9, with concurrent primary and secondary mutational sites being common. A smaller subset of GIST tumors are instead driven by mutations in the related tyrosine kinase, platelet-derived growth factor receptor-α (PDGFRα). The D842V mutant of PDGFRα in particular is equivalent to the

KIT D816X mutations, which are refractory to current therapies.[6]

Beyond surgical removal, treatment of GIST has been revolutionized by the application of targeted tyrosine kinase inhibitors capable of inhibiting KIT-driven proliferation. Imatinib **1** (Figure 1), an inhibitor of both c-KIT and PDGFRα, was initially approved in 2002 and granted accelerated approval in 2008 as first line adjuvant treatment following surgery.[7] Clinical trials have demonstrated a 5-year overall survival rate of 92% following 3-year therapy, compared with 82% for those taking the drug for one year. However, up to 20% of GIST

Table 1. Growth Inhibition Potency of GIST Treatments in KIT Mutant Ba/F3 Lines and Effect on Tel-KDR[a]

		Ba/F3 GI$_{50}$ (μM)				
compd	phase	parental	exon 11 del + V654A	exon 11 del + D816H	exon 11 del + T670I	KDR
1, imatinib	approved 1st line	>10	0.393	0.535	>10	>10
2, sunitinib	approved 2nd line	4.789	0.006	0.398	0.005	0.033
3, regorafenib	approved 3rd line	9.953	0.231	0.290	0.033	0.114
4, ripretinib	ongoing clinical trials	8.037	0.031	0.013	0.037	0.098
5, avapritinib	ongoing clinical trials	4.075	0.292	0.017	0.860	4.952

[a]All activity data are reported in μM and are the mean of at least $n = 2$ determinations and have SEM within 0.2 log units.

patients exhibit primary resistance to imatinib, and many patients taking imatinib will eventually relapse due to secondary mutations that are unresponsive to therapy, although in some case higher doses of the drug may prove effective.[8] In 2006, the FDA approved multitargeted kinase inhibitor sunitinib **2** as a second line treatment for GIST patients who are refractory to or intolerant of imatinib therapy. In these patients, time-to-tumor progression of sunitinib-treated patients was superior to that of placebo-treated patients.[9] A second multitargeted kinase inhibitor, regorafenib **3**, was approved as third line therapy in 2013 for patients with GIST that is not amenable to surgery and is refractory to both imatinib and sunitinib. Approval was again based upon improved progression free survival (PFS) versus placebo.[10] Despite the availability of these targeted agents, many clinically observed mutants of c-KIT remain unresponsive, and there remains a significant unmet need in this disease for agents with a much broader mutant KIT inhibition profile. The tolerability of sunitinib and regorafenib therapy, while clinically manageable, may also present challenges.[11] Toxicities associated with their multitargeted kinase inhibition profile can lead to dose reductions and drug holidays, which may in theory exacerbate emergence of further resistant clones. Potent inhibition of VEGFR in these agents is associated with significant high-grade hypertension, among other significant toxicities.[12]

CHEMISTRY

The synthesis of inhibitors **15** and **16** (Table 2) and related analogues **17−21** (Table 3) has been previously described.[13−16] A representative synthesis of compound **44** is shown in Scheme 1, with detailed experimental conditions for additional compounds available as Supporting Information. Accordingly, copper-catalyzed cycloaddition of ethyl azidoacetate **6** with 3-methylbut-1-yne gives triazole **7** which was hydrolyzed to carboxylic acid **8**. Amide coupling of **8** with a BOC-protected bis-aniline gave **9**, and removal of the protecting group afforded aniline **10**. Starting from difluorocyanophenol **11**, alkylation gave methoxyethyl ether **12**, and displacement of one fluoro atom with ammonia under microwave heating gave aniline **13**. This was converted to the dimethylformimidamide cyclization precursor **14** and condensation of this with prepared aniline **10** in acetic acid gave **44**, synthesizing the quinazoline and introducing the C4 group concomitantly.

RESULTS AND DISCUSSION

In order to screen for broad spectrum mutant c-KIT inhibitors with low potential for hypertension, we established a panel of Ba/F3 cell lines expressing a variety of clinically relevant secondary mutants of c-KIT, spanning the ATP binding sequence (V654A, T670I gatekeeper) and the A-loop (D816H, D820A, D823Y, and others) all on a background of a primary exon 11 deletion (of amino acids 557 and 558),

together with a line expressing Tel-KDR to monitor selectivity over KDR (VEGFR2). In this latter line, KDR is expressed as a fusion protein with a Tel sequence at the N-terminus, resulting in constitutive kinase activity. We chose exon 11 deletion as the primary mutation and the backbone for all the secondary mutations since two-thirds of GIST tumors harbor mutations in exon 11. Exon 11 deletions are associated with a shorter progression-free and overall survival in comparison to the other exon 11 mutations. In particular, deletions involving codon 557 and/or codon 558 are associated with malignant behavior.[17,18] Proliferation of these cell lines is dependent upon the introduced construct for growth, and so to monitor for nonspecific effects on viability in these cells, a parental Ba/F3 line (no introduced construct) is run in parallel. Engineered cell lines including Ba/F3 have been shown previously to faithfully mimic clinical efficacy of various agents in GIST.[19,20] It is notable that all approved therapies are type II kinase inhibitors, binding to the DFG-out kinase form, and in particular, c-KIT is one of only a small number of kinases that prefers to exist in the DFG out form in its ground state.[21] Additionally c-KIT has an unusual activation profile in that the activation loop seems not to require presence of phosphate,[22] and as type II inhibition in general is difficult to reproduce in biochemical assays, given reliance on the activation state, we viewed a cellular cascade as preferred for hit finding activities. Profiling of the various approved therapies in these lines is informative (Table 1). In line with clinical experience, **1** shows only modest activity against exon 11 deletion + V654A and D816H and no activity at all against the gatekeeper T670I mutation. Sunitinib **2** is potent against V654A and T670I but has weak activity against D816H. Regorafenib **3** is potent against the T670I mutant but is rather modest against the others, and both **2** and **3** show potent inhibition of the Tel-KDR line consistent with their potent effect on VEGFR2. Beyond these approved agents, additional compounds are currently undergoing clinical trials in GIST patients, aimed at targeting mutants of KIT not currently addressed in the clinic, with secondary D816H being a particularly refractory example. Ripretinib (DCC-2618), **4**, is a potent pan-KIT and PDGFR inhibitor from Deciphera Pharmaceuticals and shows broad inhibition across this mutant panel.[23] It is also a potent inhibitor of the Tel-KDR line however, and indeed grade 3/4 hypertension has been reported in a recent phase 1 clinical study of this compound.[24] Avapritinib (BLU-285), **5** from Blueprint Medicines is a potent inhibitor of KIT exon 17 mutations including D816 variants and also PDGFR.[25] In this panel it potently inhibits exon 11 deletion + D816H, although it is weaker against V654A and T670I. It has good selectivity for Tel-KDR, but a moderate signal in the parental line may reflect other kinase activities for this agent.

We have previously reported on efforts to develop type II quinazoline based inhibitors of both PDGFR and VEGFR that culminated in the discovery of AZD2932, **15**.[26] Follow-up work

Table 2. Growth Inhibition Potency of Literature AZ PDGFR Inhibitors in KIT Mutant Ba/F3 Lines and Effect on KDR[a]

compd			Ba/F3 GI$_{50}$ (μM)		
	parental	exon 11 del + V654A	exon 11 del + D816H	exon 11 del + T670I	KDR
15, AZD2932	>10	0.012	0.070	0.004	0.093
16	4.289	0.685	0.786	1.918	2.674

[a]All activity data are reported in μM and are the mean of at least $n = 2$ determinations and have SEM within 0.2 log units.

Table 3. SAR of KIT Mutant Ba/F3 Lines and Effect on Tel-KDR Selectivity[a]

compd	X	Y	Z	R	Ba/F3 GI$_{50}$ (μM)				
					parental	exon 11 del + V654A	exon 11 del + D816H	exon 11 del + T670I	KDR
17	N	CH	NH	H	>10	0.337	2.592	0.078	3.595
18	N	CH	O	MeO	>10	0.008	0.026	0.012	0.442
19	N	N	O	MeO	>10	0.021	0.176	0.060	8.030
20	CH	N	O	MeO	>10	0.013	0.027	0.061	3.924
21	CH	CH	O	MeO	>10	0.006	0.008	0.007	0.077

[a]All activity data are reported in μM and are the mean of at least $n = 2$ determinations and have SEM within 0.2 log units.

has also been described aimed at generating a PDGFR-selective agent from this template which led to quinoline **16** (compound **23** in this referenced work).[27] We reasoned that such inhibitors of PDGFR might show inhibition of some KIT mutants due to the close homology of KIT and PDGFR and the precedent established by compounds like **1**. What was not clear however is whether the broad and selective profile we desired would be achievable; the imatinib precedent also establishes that potent PDGFR inhibitors do not necessarily lead to broad activity against KIT mutants. Testing of **15** in this panel (Table 2) highlighted that AZD2932 did indeed show the desired broad spectrum of inhibition but that it also carried potent KDR activity, as it was designed to (encouragingly, no adverse signal was seen in the parental line, suggesting little off target activity). Conversely, the PDGF-selective compound **16**, despite weak effects on the KDR cell line, was a poor inhibitor of KIT mutants and also showed some activity in the parental line. The challenge then was to understand if the potent activity of analogues like **15** could be combined with good selectivity against KDR seen for **16**, and work that led to the latter had highlighted the importance in the nature of the central phenoxy ring and terminal heterocycle as being important drivers of KDR selectivity. Compound **17** in which the phenoxy group is replaced with an anilino linker loses potency against all KIT

mutants and also KDR (Table 3). The drop in potency against secondary A-loop mutant D816H is almost identical to the drop in KDR potency (37- versus 39-fold) in this instance. Adding a meta-methoxy group to the phenoxy ring in **18** results in maintenance of KIT potency with a modest improvement in KDR selectivity, in line with SAR previously reported for this series (selectivity of D816H over KDR is 17-fold, compared with almost parity for **15**). Conversion of the central phenyl ring of **18** into a meta-pyridine **19** results in significant diminishment of KDR potency and greater selectivity over D816H at 45-fold, although this does come with weaker overall D816H potency at 176 nM. Transposition of this into its quinoline analogue **20** results in restoration of KIT mutant potency and concomitant enhancement of selectivity over KDR (145-fold). The final compound in this matrix, **21**, combines the potent quinoline hinge binder with the meta-methoxy phenol linker of **18** to give single digit nanomolar inhibition of the three KIT lines, although in this instance KDR selectivity has been substantially impacted. Testing of additional compounds available from the original PDGFR program highlighted that other substituted end ring heterocycles such as the 3-methylpyrazole found in **16** were not tolerated in c-KIT and so could not be used to drive further levels of KDR selectivity as had been done previously (data not shown).

In order to rationalize the observed selectivity margins for compounds **17−21**, we obtained X-ray crystal structures for compound **18**, bound to the kinase domain of both wild type KIT and KDR (see Supporting Information for details). We did not attempt to crystallize in multiple KIT mutants, since we observed broad mutant selectivity over KDR and therefore reasoned that selective motifs, if apparent, would be revealed by contacts in the X-ray construct of KIT. There is high homology between KIT and KDR wild type sequences; the sequences are 56% identical in the kinase domains used for crystallography. A key difference between KIT and KDR lies in the gatekeeper residue, which is T670 in KIT and V916 in KDR. Other differences are more conservative, such as for hinge residues, which are Y672 (KIT) and F918 (KDR). The binding modes of **18** in the overlaid kinase domains are shown in Figure 2. The
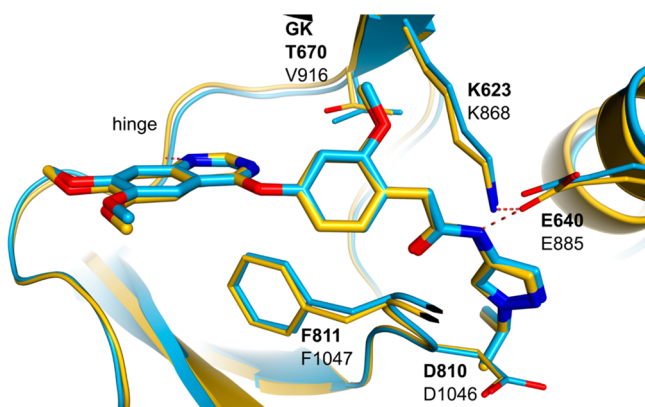

Figure 2. Kinase domains of KIT and KDR, overlaid on the binding site of compound **18**. The KIT structure is colored yellow with labels in bold typeface, the KDR structure in blue with normal typeface. Side chains are shown for the DFG motif and the catalytically important Glu-Lys pair, as well as the gatekeeper (GK) residue. PDB codes are 6GQJ and 6GQO.

binding poses are remarkably similar in the two kinases, with very few contacts to nonconserved residues. The orientation of this ligand is as expected for a type 2 kinase inhibitor. The isopropyl group binds into the DFG pocket, with no distinction between KIT and KDR, and the quinazoline nitrogen binds to the hinge. The two methoxy groups project out into solvent. We

speculate that the modest selectivity appears to arise from a less favorable orientation of the central phenyl ring with respect to the gatekeeper V916 side chain of KDR, relative to T670 in KIT. The orientation of the phenyl is dictated by the methoxy substituent and hinders a binding mode which could optimize packing to V916 of KDR. The bound ligand creates a poorly solvated cavity between ligand and gatekeeper, which can be ameliorated in KIT by the more polar Thr side chain, with a favorable interaction between quinazoline nitrogen and side chain hydroxyl.
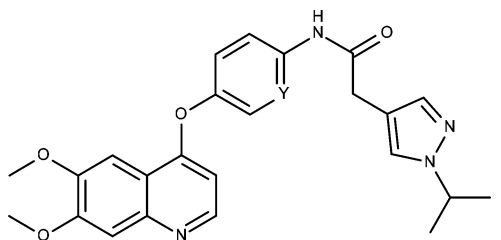
We were motivated to explore the impact of reversing the acetamide linker in this series and so made reversed acetamide matched pairs to simple analogues available from the original PDGFR program (Table 4). Compound **22** is the *N*-ethylpyrazole analogue of **15**,[16,26] and its reversed acetamide counterpart **23** encouragingly had a largely similar profile. Selectivity against KDR is moderately enhanced in the reversed acetamide, 6-fold from roughly 1:1 over D816H, while affinity for the T670I gatekeeper is most severely impacted (down 20-fold), activity against V654A and D816H is largely similar. Analogue **24**, in which the central ring is appended with a methoxy group, is a first indication however that the SAR that was apparent in the original acetamide series does not transfer when the acetamide is reversed. Whereas previously a 17-fold improvement in selectivity was noted, here selectivity is unchanged, as is potency across all the mutants; methoxy on the central ring appears to offer no advantage. A similar breakdown in SAR was seen for introduction of a central pyridine ring (Table 5). In the quinoline matched pairs **25** (phenyl) and **26** (pyridine), introduction of nitrogen causes a significant drop in all KIT potencies except T670I, and although KDR potency is weaker, selectivity is unchanged.

We obtained a matched pair of X-ray structures for compound **23**, as shown in Figure 3. In this case, we observed ligand binding modes that are slightly offset in the vicinity of the hinge and gatekeeper, with the pendant ethyl group of the pyrazole ring coincident in the two binding sites. This suggests that interaction in the DFG pocket is dominant for this scaffold but that selectivity arises once again from the gatekeeper pocket. Since **23** is a quinazoline, the N3 atom is available to chelate a water molecule, which is now visible in the KIT structure (shown as a red sphere). There is no water observed in KDR

Table 4. Impact of Reversing the Acetamide Linker on KIT and KDR Potency[a]

Acetamide   **Reversed acetamide**

| compd | amide | R | Ba/F3 GI$_{50}$ (μM) | | | | |
			parental	exon 11 del + V654A	exon 11 del + D816H	exon 11 del + T670I	KDR
22	acetamide	H	>10	0.044	0.488	0.007	0.680
23	reversed acetamide	H	>10	0.021	0.250	0.141	1.615
24	reversed acetamide	MeO	>10	0.078	0.251	0.086	2.551

[a]All activity data are reported in μM and are the mean of at least *n* = 2 determinations and have SEM within 0.2 log units.
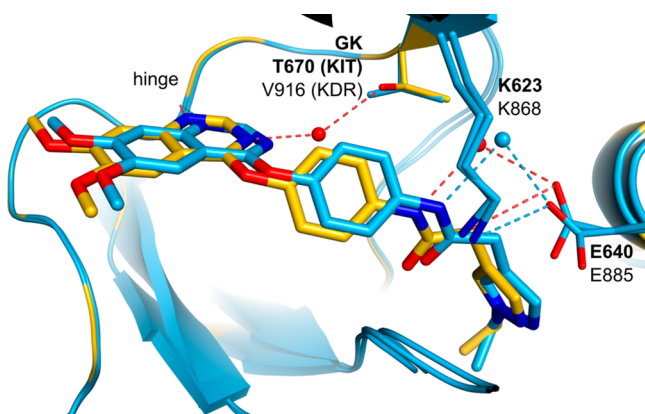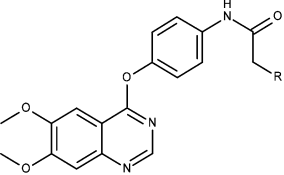
Table 5. Impact of Reversing a Pyridine Linker on KIT and KDR Potency[a]

		Ba/F3 GI$_{50}$ (μM)				
compd	Y	parental	exon 11 del + V654A	exon 11 del + D816H	exon 11 del + T670I	KDR
25	CH	>10	0.026	0.047	0.007	0.082
26	N	>10	0.150	0.518	0.008	0.761

[a]All activity data are reported in μM and are the mean of at least n = 2 determinations and have SEM within 0.2 log units.

Figure 3. Kinase domains of KIT and KDR, overlaid on the binding site of reversed acetamide compound **23**. KIT protein ribbons are colored by sequence identity, with blue residues identical and yellow nonidentical to KDR. The binding mode is offset between the two kinases, but there are still very few contacts to nonconserved residues. Water molecules are shown as red speheres in KIT and blue spheres in KDR. A water molecule is observed in the KIT structure but is absent from the KDR structure. Selectivity appears to arise from less favorable orientation of the central aromatic ring against the V916 side chain of KDR, relative to the solvated T670 side of KIT. In addition, the hinge interaction in KDR seems to be less optimal than for KIT. PDB codes 6GQK and 6GQP.
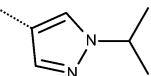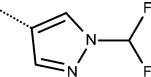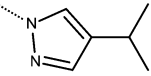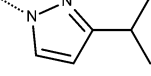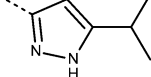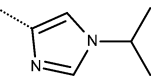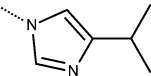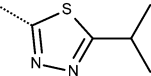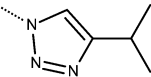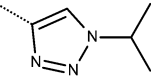
here, our assumption being that this would be very unstable when packed against the V918 side chain. Instead, in KDR, the ligand partially occupies the solvent pocket in preference to water, weakening both the hinge interaction and the packing against the gatekeeper residue. We assumed that a similar solvation stabilization of **18** is possible, but this was not observed in our X-ray structures (Figure 2). The nitrogen position in the reversed acetamide precludes a direct hydrogen bond with the glutamic acid chain (E640/E885), in contrast to that observed in the normal acetamide. This region of the complex remains quite polar, however, so that a crystallographic water is observed to bind in both CKIT and KDR, as shown in Figure 3. The water appears to mediate a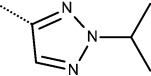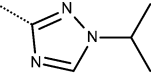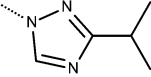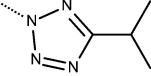n interaction between acid side chain and ligand. The water positions are almost coincident in CKIT and KDR so that we could not use this interaction to explain selectivity between the two proteins.

With previous SAR unsuited to driving the greater levels of potency and selectivity required, we turned attention to varying the end-ring of the reversed acetamide using a series of aromatic acetic acids available through an in house building block

initiative.[28] Table 6 shows the impact of varying the nature of the five-membered heteroaromatic portion of the molecule, and here we focused on finding the optimal balance of exon 11 deletion + D816H potency (since this appears to be the most challenging mutant to inhibit with this template) and KDR selectivity while keeping log D as low as possible. Compound **27**, serves as a useful benchmark for these changes as it is the reversed acetamide version of analogue **15**; potency and lipophilicity are good, but KDR selectivity is modest. Switching the isopropyl group to a difluoromethyl **28** gives a largely similar profile. Reversing the pyrazole so that connection to the acetamide is via an N-link as in analogues **29** and **30** provides compounds with improved KDR margin but comes at the expense of increased lipophilicity. The last pyrazole in this set **31** with a free NH gives a very potent D816H inhibitor, reasonable selectivity but again with higher than desirable log D of 3.6. A C-linked imidazole **32** sees a drop in activity and selectivity, whereas linking through nitrogen as in **33** gives a potent and selective inhibitor. A thiadiazole **34** is potent but has only 10-fold margin to KDR and log D of 3.3. We also examined a series of 1,2,3-triazoles **35**−**37**. The pick of these appears to be triazole **35**, which combines good potency (19 nM) and selectivity with an acceptable log D of 2.9. Triazole **36** is less potent and triazole **37** less selective than **35**. In related 1,2,4-triazoles, compound **38** sees potency significantly diminished, and analogue **39**, although an improvement, is not superior to any 1,2,3-triazole. Completing this set, the tetrazole **40** shows a reasonable balance of potency, selectivity, and lipophilicity. From this work N-linked triazole **35** emerged as the most favorable end-ring, although further increases in selectivity were desired.

The notable gains in potency and selectivity for these heterocyclic end groups prompted us to solve a further X-ray matched pair, this time for compound **35**. As seen in Figure 4, the binding mode at the hinge and gatekeeper is less offset than for **23** (Figure 3), but this appears to be due to a different orientation in the DFG pocket. The pendant isopropyl group packs against the V898 side chain of KDR but projects further from the pocket in KIT due to a larger I653 side chain at the equivalent position. This results in a significant offset of the triazolo group between KIT and KDR and a different orientation for the isopropyl group. The triazole dipole is oriented toward bulk water, as we would expect for a broadly hydrophobic pocket and consequently solvent mapping suggests that the triazolo motif occupies a more favorable position in KIT relative to KDR.[29] In KDR, it appears to be buried too far into the pocket to optimize packing against V898, precluding effective solvation of

Table 6. Exon 11 Deletion + D816H KIT Mutant Potency and KDR Selectivity for a Series of Aromatic Acetamides[a]

ID	R	exon 11 del D816H Ba/F3 GI$_{50}$ (μM)[1]	Fold KDR selectivity	LogD[2]
27		0.021	5.9	2.9
28		0.087	4.4	2.7
29		0.021	11.4	3.8
30		0.035	23.5	3.5
31		0.009	15.6	3.6
32		0.240	4.6	2.8
33		0.021	34.1	3.3
34		0.026	9.9	3.3
35		0.019	32.2	2.9
36		0.111	12.6	2.6
37		0.075	9.3	2.9
38		1.369	3.9	2.3
39		0.175	15.9	2.6
40		0.042	15.7	3.0

[a]Footnotes: [1]All activity data are reported in μM and are the mean of at least $n = 2$ determinations and have SEM within 0.2 log units. [2]Measured log D at pH 7.4.

the exposed dipole. This also explains why compound **27** is less selective, since the pyrazole end group can present a hydro-phobic atom in the KDR pocket. Combining isopropyl with a heterocycle with significant dipole, such as triazolo, gives a
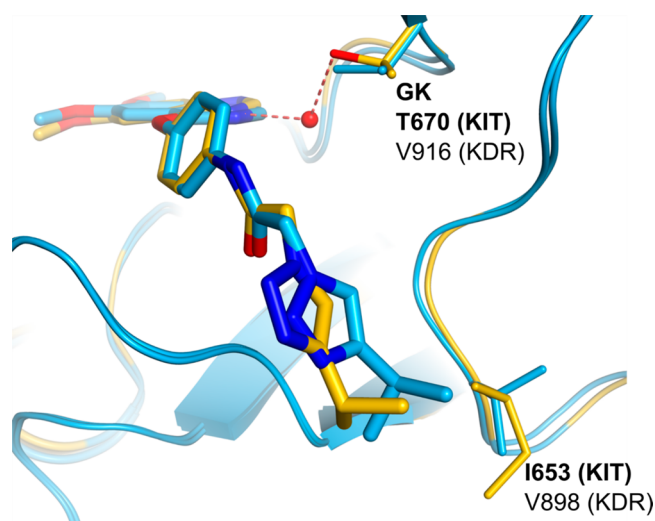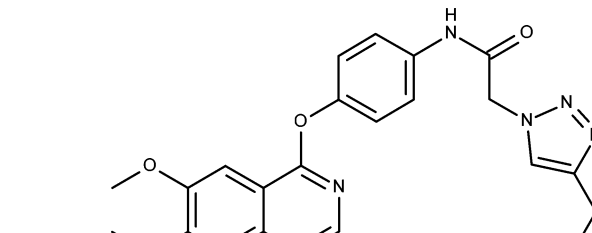
Figure 4. Kinase domains of KIT and KDR, overlaid on the binding site of compound **35**. KIT protein is colored by sequence identity, with blue residues identical and yellow nonidentical to KDR. The binding mode at hinge and gatekeeper is less offset than in previous examples, but attention now shifts to nonconserved residues in the DFG pocket. The isopropyl group clashes with I653 in KIT but is accommodated by the smaller V898 side chain of KDR. The triazolo motif is more buried in KDR as a result, and we hypothesize that this results in a desolvation penalty that increases affinity to KIT for this ligand and for this general DFG pocket motif. PDB codes 6GQL and 6GQQ.

binding orientation that is optimal for solvation in the KIT pocket and suboptimal for KDR. When coupled with a selective gatekeeper motif and the bound water (also visible in Figure 2), we then see a significant selectivity gain.
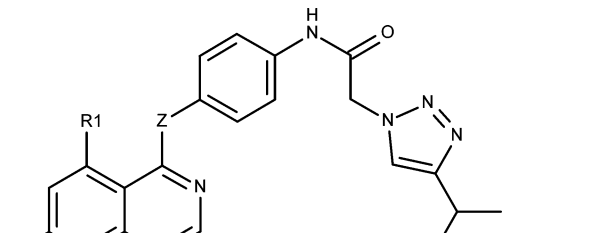
We next turned our attention to examining substituents at the quinazoline 5-position, since this is a region that projects toward the ribose pocket of ATP, an area of fruitful optimization in quinazoline-based kinase inhibitors historically.[30] Compound **35** is a potent inhibitor of all three KIT mutants (Table 7). Migration of the 6-methoxy group to the 5-position **41** does not change the profile a great deal; a modest 2- to 3-fold drop in potencies is observed across all cell lines, and certainly KDR

selectivity is not further enhanced. Despite this, we explored the impact of switching the 4-phenoxy linker back to a 4-anilino linker with compound **42**. We had seen earlier in the normal amide series, compound **17** with an anilino linker lost significant activity against KIT mutants, although we speculated that the potential lone pair clash between the adjacent oxygen atoms (at C4 and C5) in **41** might impact the optimal C4 substituent vector and that reversion to an NH linker, which could internally hydrogen bond to the 5-methoxy group, might be more favorable. In the event, the aniline linked **42** was as effective at inhibiting KIT mutants as its phenoxy counterpart but with much improved selectivity over KDR (113-fold compared with 24- and 32-fold for **41** and **35** respectively). It is striking that two structural changes that individually lead to a worsened profile, when combined together, are able to drive a significant benefit. Exploration of alternative substituents at C5 led to 5-fluoro analogue **43** which maintains KIT potency and leads to even greater KDR selectivity of at least 400-fold. Fluorine was selected as an alternative to methoxy that could, potentially at least, form an internal hydrogen bond to the C4 NH. This compound however unexpectedly suffered from adverse physicochemical properties, in particular high plasma protein binding of 99.7% bound, an issue that was directly addressed by variation of the C7 substituent. Compound **44**, containing a C7 methoxyethoxy group, was determined to have the optimal balance between KIT mutant potency and KDR selectivity from this work and was selected for further profiling. It demonstrates very potent growth inhibition across KIT mutant cell lines with good KDR margin, not quite as selective as **43**, but significant improvements in physicochemical and ADME properties (Table 8). Despite a low solubility consistent with its chemical structure and neutral chemotype, permeability in Caco2 cells is very high. This, coupled with its low in vitro clearance in hepatocytes, leads to excellent observed in vivo pharmacokinetics in preclinical species. Bioavailability is high and clearance low across all of mouse, rat, and dog. Volume of distribution is low consistent with the neutral structure. A structure of **44** bound in KIT was obtained and shows features consistent with the preceding X-ray structures (Figure 5). There is a bound water at the gatekeeper, promoting selectivity, and the triazolo group binds in a similar

Table 7. SAR of 5-Substituted Quinazolines[a]
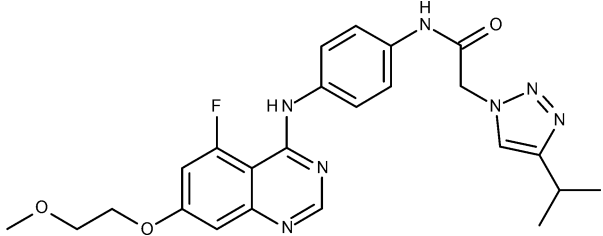
				Ba/F3 GI$_{50}$ (μM)				
compd	Z	R1	R2	parental	exon 11 + del V654A	exon 11 + del D816H	exon 11 + del T670I	KDR
35				>10	0.003	0.019	0.017	0.612
41	O	MeO	Me	>10	0.007	0.050	0.055	1.222
42	NH	MeO	Me	>10	0.003	0.048	0.107	5.408
43	NH	F	Me	>10	0.002	0.025	0.068	>10
44	NH	F	MeO(CH$_2$)$_2$	>10	0.003	0.009	0.016	1.378

[a]All activity data are reported in μM and are the mean of at least $n = 2$ determinations and have SEM within 0.2 log units.

Table 8. Detailed ADME Characteristics of Compound 44

parameter	value
log D at pH 7.4[a]	3.0
solubility at pH 6.5 (μM)[b]	6
permeability Caco2 A to B (1×10^{-6} cm/s)[c] (efflux ratio)	62.3 (2.6)
plasma protein binding % free (mouse, rat, dog, human)	4.9, 2.2, 6.8, 3.5
hepatocyte Cl_{int} ((μL/min)/10^{-6} cells) (mouse, rat, dog, human)	5, 17, <1, <1
hERG IC_{50} (μM)	>33.3
pharmacokinetics Cl (mL min^{-1} kg^{-1}), Vd_{ss} (l/kg), $t_{1/2}$ (h), F (%)	
mouse[d]	7, 0.7, 2, 100
rat[e]	8, 0.6, 3, 79
dog[f]	2, 0.3, 4, 69

[a]Measured log D at pH 7.4. [b]Solubility of crystalline form A measured in pH 6.5 phosphate buffer at 37 °C. [c]Permeability measured at pH 6.5 using 10 μM solution of compound. [d]PK in CD1 mouse following oral (21 μmol/kg) and iv doses (10 μmol/kg). [e]PK in Han Wistar rat following oral (2.1 μmol/kg) and iv doses (1 μmol/kg). [f]PK in dog following oral (2.1 μmol/kg) and iv doses (1 μmol/kg). Half lives reported are from oral dosing.
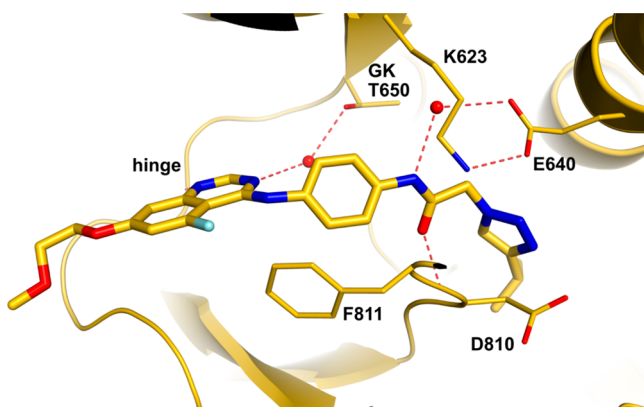

Figure 5. Cocrystal structure of **44** bound to c-KIT (resolution 2 Å). Water molecules are shown as red spheres. PDB code is 6GQM.

place in the DFG pocket as was seen for compound **35**. The extended C7 side chain protrudes from the active site out into solvent.

Compound **44** was compared against the approved and investigational KIT inhibitors outlined in Figure 1 against a much broader panel of KIT mutant Ba/F3 cell lines expressing a diverse set of clinically relevant primary and secondary mutations, including a small panel of PDGFR driven lines relevant in subsets of GIST (Table 9). It shows very potent growth inhibition of nearly all mutants tested and, consistent with its lineage and other KIT inhibitors, maintains potent activity against PDGFR, including the clinically GIST-relevant D842V mutant. It maintains low nM potency against secondary mutations on a primary background of either exon 9 insertion or exon 11 deletion and is sub-10 nM in 12 of the 19 lines examined. Conversely, imatinib **1** is a relatively poor inhibitor of

these diverse KIT mutants, showing significant activity against a primary mutation of exon 11 insertion and V560D, together with PDGFR only. Sunitinib **2** carries greater KIT mutant activity than **1** and shows potent activity against secondary mutations of ATP binding pocket but is much weaker against clinically relevant mutations of the A-loop. Third line agent regorafenib **3** is a little more potent against these mutations but against many of the others appears inferior to sunitinib **2**. The investigational agent ripretinib **4** does show potent and broad-spectrum activity against the KIT mutants in this panel, although with the exception of its PDGF activity it is only superior to **44** in a single mutant (primary D816V). As previously indicated, the margin to KDR for this agent is significantly eroded relative to **44** (only 8-fold compared with 153-fold against exon 11 insertion + D816H). Avapritinib **5** is potent against certain subsets of KIT mutants, notably D816/820 and PDGFR, although it lacks potent activity against mutants such as V654A and T670I. Consistent with our goals, compound **44** demonstrates equivalent or superior growth inhibition in all but 2 of the 19 cell lines investigated when compared to agents **1**−**5**.

In order to ensure that the broad KIT mutant inhibition profile observed had not been achieved at the expense of general kinome selectivity, compound **44** was assessed in an extended panel of human kinase binding assays alongside clinical agents **1**−**5** (Figure 6). In this panel of 379 human kinases, activity was compared by screening at a single, relatively high concentration of 1 μM, which is far in excess of the potency seen in the Ba/F3 GI_{50} assays. Encouragingly compound **44** compares well to these other inhibitors, with an overall selectivity similar to that of imatinib **1** and avapritinib **5**. Both sunitinib **2** and regorafenib **3** show increased activity across this panel, with exploratory agent ripretinib **4** showing a spectrum of activity between these two approved therapies.

A key advantage of using Ba/F3 cell lines in the cascade optimization is that these allow a direct assessment of potency translation in vivo. The activity of compound **44** in a series of mouse allograft tumor models using these Ba/F3 lines was assessed and compared to current standards of care relevant to each mutant (Figure 7 and Table 10). As expected **1** shows only limited activity in the exon 11 del/D816H background a mutation to which it is refractory. Regorafenib **3** fares better and is able to drive regression of tumor volume at a dose of 100 mg/kg q.d., although this is surpassed by **44** at a dose of 20 mg/kg b.i.d. A dose response is evident in that **44** at a dose of 2 mg/kg b.i.d. shows no impact on tumor size. Sunitinib **2** was not assessed in this model as it is inactive against the D816H mutant. In an exon 11 del/V654A allograft however and consistent with its clinical use, **2** showed strong regressions at 80 mg/kg q.d. and was matched by **44** at a dose of 20 mg/kg b.i.d. (and even as low as 2 mg/kg **44** was highly effective). Imatinib showed moderate activity in this study. Figure 8 shows the pharmacodynamic response to **44** in the D816H model at the top 20 mg/kg dose tested with the impact on levels of pKIT and downstream markers pERK and pAKT, together with a timecourse of compound free cover levels above IC_{90} in the same study. Following a single dose, high free cover over target is achieved and is associated with complete suppression of pKIT and downstream markers out to 8 h. As compound is cleared and cover declines, these signals recover, although recovery is not complete even at 24 h.

Table 9. Comparison of Mutant KIT and PDGF Potencies for Compound 44 with Approved and Investigational GIST Therapies 1−5

gene	primary mutation	secondary mutation	KIT inhibitor Ba/F3 GI$_{50}$ (μM)					
			44	1	2	3	4	5
KIT	exon 9 ins[a]		0.002	0.192	0.007	0.114	0.034	0.167
	exon 9 ins[a]	V654A	0.022	3.947	0.012	1.270	0.205	0.751
	exon 9 ins[a]	D816H	0.051	2.749	0.584	0.833	0.078	0.069
	exon 11 del[b]		0.001	0.017	0.004	0.021	0.004	0.078
	exon 11 del[b]	V654A	0.003	0.392	0.006	0.234	0.032	0.292
	exon 11 del[c]	V654A	0.008	1.523	0.024	0.943	0.130	0.117
	exon 11 del[b]	T670I	0.016	9.689	0.005	0.034	0.038	0.860
	exon 11 del[b]	D816H	0.009	0.537	0.400	0.297	0.013	0.017
	exon 11 del[b]	D820A	0.003	0.216	0.214	0.063	0.006	0.019
	exon 11 del[b]	Y823D	0.014	0.669	0.782	0.094	0.014	
	exon 11 del[b]	N822K	0.003	0.223	0.271	0.049	0.004	0.034
	exon 11 del[b]	A829P	0.004	0.312	0.430	0.047	0.003	0.028
	V560D		0.001	0.070	0.027	0.108	0.023	0.042
	V560D	V654A	0.007	0.701	0.007	0.549	0.075	0.427
	V560D	D816H	0.018	1.191	0.696	0.834	0.048	0.029
	D816V		0.971	9.930	0.638	2.371	0.037	0.008
PDGFR	Tel-PDGFRα		0.001	0.046	0.030	0.051	0.040	0.034
	Tel-PDGFRβ		0.008	0.102	0.114	0.029	0.045	0.022
	V561D[d]	D842V[d]	0.022	0.567	0.631	0.522	0.188	0.010

[a]AY502−503 insertion at exon 9. [b]Deletion of 557−558 at exon 11. [c]Deletion of 560−578 at exon 11. [d]PDGFRα.
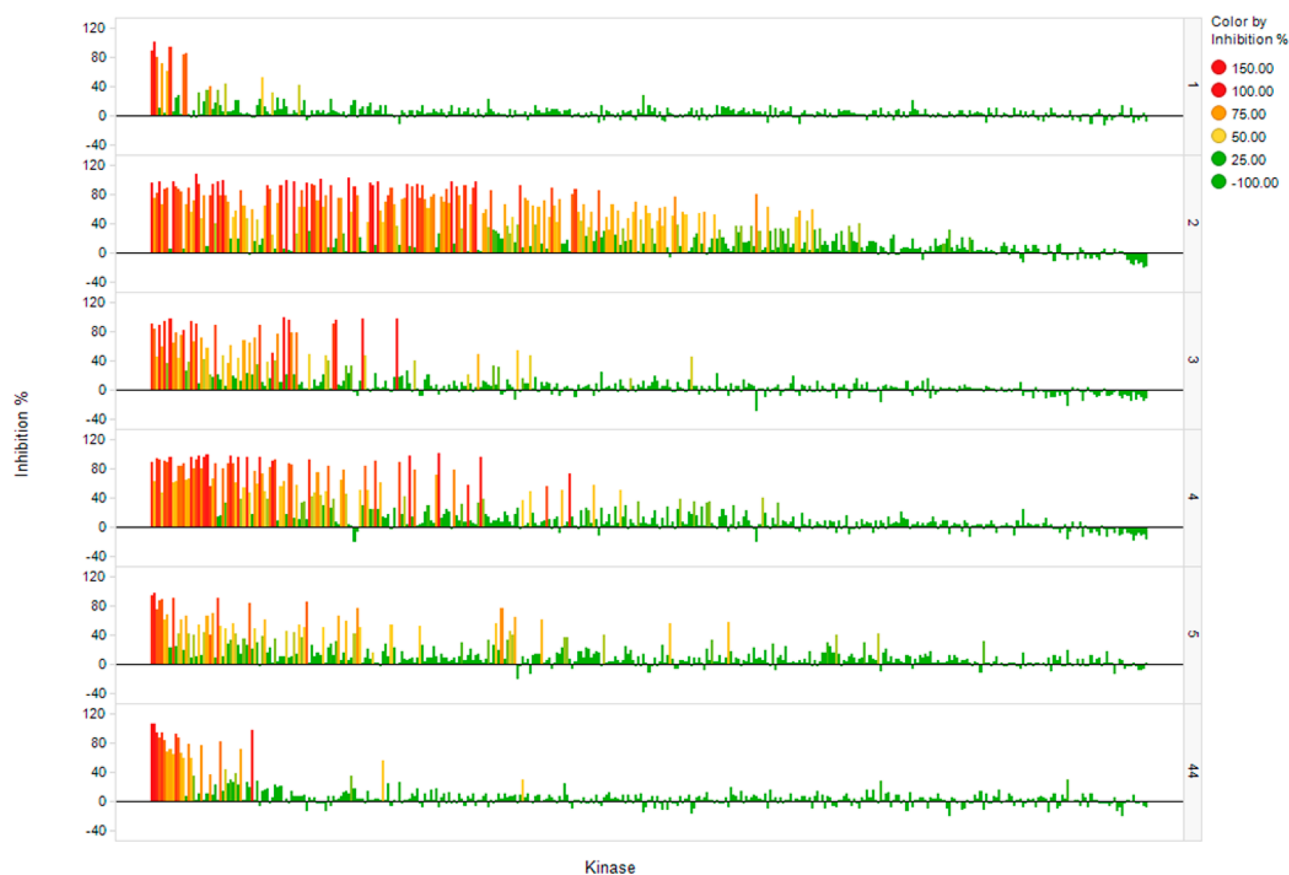

Figure 6. Comparative selectivity of inhibitors **1−5** and **44** in a panel of 379 human kinases run in the SelectScreen kinase panel at ThermoFisher Scientific at a single concentration of 1 μM. These data are available as individual annotated kinase data points in Supporting Information.

◼ CONCLUSIONS

Having established as a goal the challenging profile of an inhibitor capable of addressing all diverse KIT mutants, this has been realized in a series of type II quinazoline kinase inhibitors. Identification of a series of kinase inhibitors from an historical project combined with structure-based insights allowed for rapid optimization in particular of both mutant and kinase selectivity,
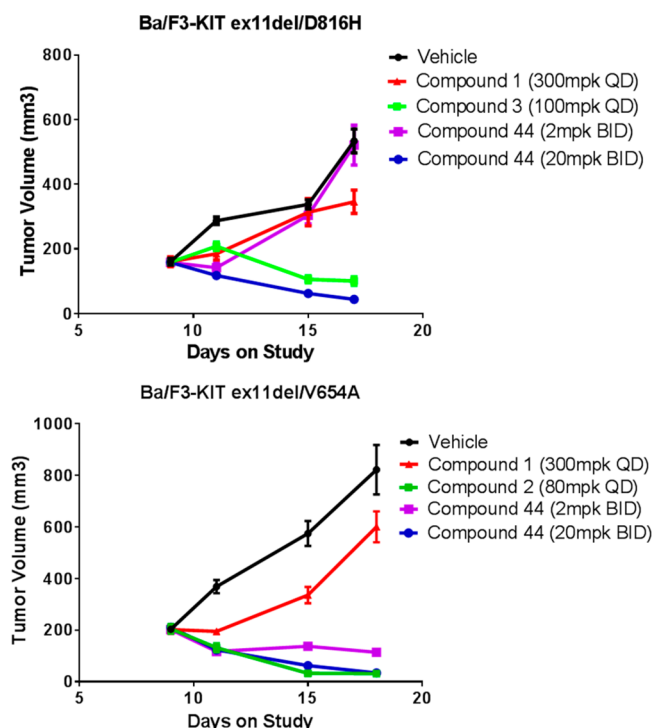
Figure 7. In vivo efficacy of KIT inhibitors in mouse allograft disease models. Upper panel: imatinib and regorafenib versus **44** in an exon 11 del/D816H model. Lower panel: imatinib and sunitinib versus **44** in an exon 11 del/V654A model. Doses for standards of care were selected to best represent their clinically relevant doses.

not just against KDR but the wider kinome. Despite high homology between KIT and antitarget KDR, we propose that subtle differences in the way each is able to accommodate and in particular solvate the liganded structures are key to the enhanced selectivity seen. The preclinical in vivo efficacy of **44**, now designated AZD3229, is encouraging, particularly in relation to current standards of care and may hold promise in the future treatment of GIST patients. Further data relating to the pharmacological activity of AZD3229, including assessment of required margins over KDR to ensure no hypertensive effects[31] that limit current agents, will be reported in due course.

■ **EXPERIMENTAL METHODS**

Chemistry. Unless otherwise stated, commercially available reagents were used as supplied. All reactions requiring anhydrous

conditions were conducted in dried apparatus under an atmosphere of nitrogen. Flash column chromatography was performed on Merck Kieselgel silica (Art. 9385) or on reversed phase silica (Fluka silica gel 90 C18) or on Silicycle cartridges (40−63 μm silica, 4−330 g weight) or on Grace resolv cartridges (4−120 g) or on RediSep Rf 1.5 Flash columns or on RediSep Rf high performance Gold Flash columns (150−415 g weight) or on RediSep Rf Gold C18 reversed-phase columns (20−40 μm silica) either manually or automated using an Isco CombiFlash Companion system or similar system. Preparative reverse phase HPLC was performed on a Waters instrument (600/2700 or 2525) fitted with a ZMD or ZQ ESCi mass spectrometers and a Waters X-Terra or a Waters X-Bridge or a Waters SunFire reverse-phase column (C-18, 5 μm silica, 19 mm or 50 mm diameter, 100 mm length, flow rate of 40 mL/min) using decreasingly polar mixtures of water (containing 1% ammonia) and acetonitrile or decreasingly polar mixtures of water (containing 0.1% formic acid) and acetonitrile as eluents. NMR chemical shift values were measured on the δ scale [proton magnetic resonance spectra were determined using a Bruker Avance 500 (500 MHz), Bruker Avance 400 (400 MHz), Bruker Avance 300 (300 MHz) or Bruker DRX (300 MHz) instrument]; measurements were taken at ambient temperature unless otherwise specified. The following abbreviations have been used: s, singlet; d, doublet; t, triplet; q, quartet; m, multiplet; dd, doublet of doublets; ddd, doublet of doublet of doublet; dt, doublet of triplets; bs, broad signal. In general, end products were also characterized by mass spectroscopy following liquid chromatography (LCMS or UPLC); in general, reverse-phase C18 silica was used with a flow rate of 1 mL/min and detection was by electrospray mass spectrometry and by UV absorbance recording a wavelength range of 220−320 nm. Analytical UPLC was performed on CSH C18 reverse-phase silica, using a Waters XSelect CSH C18 column with dimensions 2.1 mm × 50 mm and particle size 1.7 μm). Gradient analysis was employed using decreasingly polar mixtures as eluent, for example, decreasingly polar mixtures of water (containing 0.1% formic acid or 0.1% ammonia) as solvent A and acetonitrile as solvent B. A typical 2 min analytical UPLC method would employ a solvent gradient over 1.3 min, at approximately 1 mL per minute, from a 97:3 mixture of solvents A and B, respectively, to a 3:97 mixture of solvents A and B. The reported molecular ion corresponds to the $[M + H]^+$ unless otherwise specified; for molecules with multiple isotopic patterns (Br, Cl, etc.) the reported value is the one obtained for the lowest isotope mass unless otherwise specified. Ion exchange purification was generally performed using an SCX-2 (Biotage) cartridge. Where reactions refer to the use of a microwave, one of the following microwave reactors were used: Biotage Initiator, Personal Chemistry Emrys Optimizer, Personal Chemistry Smithcreator, or CEM Explorer. Purities were assessed using LCMS by UV absorbance and ^{1}H NMR and are ≥95% unless otherwise stated.

Ethyl 2-(4-Isopropyl-1*H***-1,2,3-triazol-1-yl)acetate (7).** A 30% solution of ethyl 2-azidoacetate (**6**) in DCM (19.5 g, 45.4 mmol) was added as a solution in acetonitrile (27 mL) over 5 min to a suspension of copper(I) iodide (0.17 g, 0.9 mmol), 3-methylbut-1-yne (5.1 mL,

Table 10. Percent and Statistical Significance of Tumor Growth Inhibition and Regressions of 44 Relative to Vehicle and Standards of Care in Two Mouse Allograft Disease Models of Mutant KIT Activity

tumor	compd	dose (mg/kg)	schedule	route	% inhibition[a]	% regression[a]	p-value[b]
Ba/F3 KIT-exon 11 del/D816H	vehicle	n/a	b.i.d.	po	n/a	n/a	n/a
	1	300	q.d.	po	43	0	0.0095
	3	100	q.d.	po	>100	39	<0.0001
	44	2	b.i.d.	po	5	0	0.3818
	44	20	b.i.d.	po	>100	75	<0.0001
Ba/F3 KIT-exon 11 del/V654A	vehicle	n/a	b.i.d.	po	n/a	n/a	n/a
	1	300	q.d.	po	34	0	0.0495
	2	80	q.d.	po	>100	87	<0.0001
	44	2	b.i.d.	po	>100	44	<0.0001
	44	20	b.i.d.	po	>100	85	<0.0001

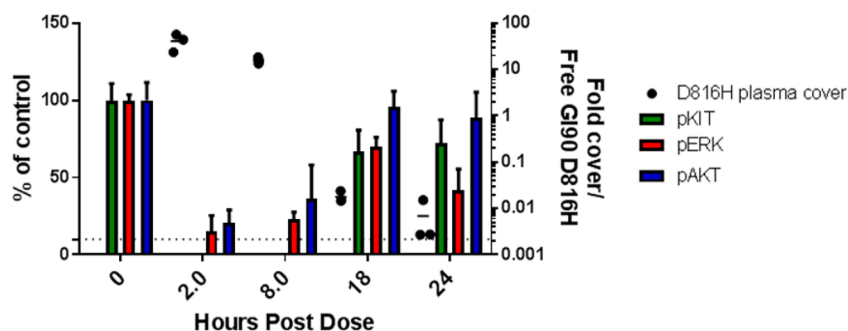[a]On last day of dosing. [b]Relative to vehicle.

Figure 8. Pharmacodynamic effect of **44** on tumor pKIT, pERK, and pAKT in an exon 11 del/D816H mouse allograft model from a single dose of 20 mg/kg po. No pKIT was detectable at $t = 2$ or 8 h. A more detailed statistical analysis of these data are available in Supporting Information.

49.9 mmol), and triethylamine (0.13 mL, 0.9 mmol) in acetonitrile (27 mL) at room temperature. The mixture was stirred for 3 days at room temperature. The mixture was concentrated and the residue was partitioned between water (150 mL) and ethyl acetate (150 mL). The aqueous layer was extracted with ethyl acetate (100 mL), and the extracts were combined with the organic layer. The combined extracts were dried and evaporated to dryness. The crude product was purified by flash silica chromatography, elution gradient 30−50% ethyl acetate in heptane. Pure fractions were evaporated to dryness to afford the title compound as a white crystalline solid (8.06 g, 90%). ^{1}H NMR (500 MHz, DMSO, 27 °C) δ 1.21 (3H, t), 1.22 (6H, d), 2.98 (1H, hept), 4.16 (2H, q), 5.30 (2H, s), 7.82 (1H, d). m/z: ES+ [M + H]$^+$ 198.

2-(4-Isopropyl-1*H***-1,2,3-triazol-1-yl)acetic Acid (8).** Lithium hydroxide hydrate (10.2 g, 242.5 mmol) was added as a solution in water (540 mL) to ethyl 2-(4-isopropyl-1*H*-1,2,3-triazol-1-yl)acetate (**7**) (15.9 g, 80.8 mmol) in THF (180 mL). The mixture was stirred for 90 min, then concentrated. The resulting aqueous solution was acidified to pH 5 with 2 M HCl and extracted with ethyl acetate (200 mL). The aqueous layer was evaporated to dryness to afford the title compound as a white solid containing LiCl (28.2 g, 100%, 48% strength), which was used without further purification. ^{1}H NMR (500 MHz, DMSO, 27 °C) δ 1.20 (6H, d), 2.92 (1H, hept), 4.59 (2H, s), 7.62 (1H, d). m/z: ES+ [M + H]$^+$ 170.

tert*-Butyl (4-(2-(4-Isopropyl-1H***-1,2,3-triazol-1-yl)-acetamido)phenyl)carbamate (9).** HATU (18.4 g, 48.3 mmol) was added to a solution of *tert*-butyl (4-aminophenyl)carbamate (8.4 g, 40.3 mmol), 2-(4-isopropyl-1*H*-1,2,3-triazol-1-yl)acetic acid (**8**) (19.4 g, 44.3 mmol), and DIPEA (10.5 mL, 60.4 mmol) at ambient temperature. The mixture was stirred at ambient temperature for 16 h. The mixture was concentrated to 75 mL volume, diluted with water (700 mL), and extracted with ethyl acetate (3 × 300 mL). The combined ethyl acetate extracts were washed with 0.5 M citric acid solution (300 mL), water (4 × 300 mL), 0.5 M NaHCO₃ solution (200 mL), water (200 mL), brine (200 mL) and dried. The solution was evaporated to dryness and the residue was recrystallized from acetonitrile to afford the title compound as a white solid (8.2 g, 57%). ^{1}H NMR (500 MHz, DMSO, 27 °C) δ 1.23 (6H, d), 1.45 (9H, s), 2.98 (1H, hept), 5.20 (2H, s), 7.38 (2H, d), 7.44 (2H, d), 7.83 (1H, d), 9.27 (1H, s), 10.31 (1H, s). m/z: ES+ [M + H]$^+$ 360.

N*-(4-Aminophenyl)-2-(4-isopropyl-1H***-1,2,3-triazol-1-yl)-acetamide (10).** 4 M hydrogen chloride in dioxane (15.3 mL, 61.2 mmol) was added to a mixture of *tert*-butyl (4-(2-(4-isopropyl-1*H*-1,2,3-triazol-1-yl)acetamido)phenyl)carbamate (**9**) (2.2 g, 6.1 mmol) in DCM (20 mL) and methanol (20 mL). The mixture was stirred at ambient temperature for 3 h, during which time an additional portion of 4 M hydrogen chloride in dioxane (8 mL, 24 mmol) was added. The mixture was evaporated to dryness and the residue dissolved in water (70 mL). This aqueous solution was added slowly to stirred 1 M potassium carbonate solution (150 mL), causing a white solid to precipitate. The mixture was stirred for 10 min at ambient temperature. The precipitate was collected by filtration, washed with water, and dried under vacuum to afford the title compound as a white solid (1.4 g, 89%) which was used without purification. ^{1}H NMR (500 MHz, DMSO, 27 °C) δ 1.23 (6H, d), 2.98 (1H, hept), 4.90 (2H, s), 5.14 (2H, s), 6.50

(2H, d), 7.20 (2H, d), 7.82 (1H, s), 9.99 (1H, s). m/z: ES+ [M + H]$^+$ 260.

2,6-Difluoro-4-(2-methoxyethoxy)benzonitrile (12). 1-Bromo-2-methoxyethane (8.4 mL, 89 mmol) was added to a stirred suspension of 2,6-difluoro-4-hydroxybenzonitrile (**11**) (11.5 g, 74.1 mmol) and potassium carbonate (30.7 g, 222.4 mmol) in DMF (175 mL). The mixture was heated to 85 °C for 5 h. The mixture was cooled to ambient temperature and was poured into water (1250 mL). The mixture was extracted with ethyl acetate (2 × 400 mL). The combined extracts were washed with water (4 × 400 mL), saturated brine (200 mL), dried and evaporated to dryness to give an orange oil. The crude product was purified by flash silica chromatography, elution gradient 20−45% ethyl acetate in heptane. Pure fractions were evaporated to dryness to afford the title compound as a white crystalline solid (16.1 g, 93%). ^{1}H NMR (500 MHz, DMSO, 27 °C) δ 3.28 (3H, s), 3.62−3.68 (2H, m), 4.21−4.27 (2H, m), 7.05−7.14 (2H, m). m/z: ES+ [M + H]$^+$ 214.

2-Amino-6-fluoro-4-(2-methoxyethoxy)benzonitrile (13). 2,6-Difluoro-4-(2-methoxyethoxy)benzonitrile (**12**) (23 g, 107.9 mmol) was split between 14 microwave vials, each containing (1.64 g, 7.7 mmol) substrate. Each batch was suspended in isopropanol (3 mL), and concentrated aqueous ammonia solution (8 mL, 3237 mmol) was added. Each vial was capped and heated to 100 °C in microwave reactors for 13 h. All batches were combined; the solid which crystallized from solution was collected by filtration, washed with water, and dried to afford the title compound as a white crystalline solid (19.6 g, 87%). ^{1}H NMR (500 MHz, DMSO, 27 °C) δ 3.28 (3H, s), 3.57−3.64 (2H, m), 4.02−4.07 (2H, m), 6.10 (1H, dd), 6.17 (1H, dd), 6.35 (2H, s). m/z: ES− [M − H]$^-$ 209.

(*E*)-*N*′-(2-Cyano-3-fluoro-5-(2-methoxyethoxy)phenyl)-*N*,*N*-dimethylformimidamide (14). 1,1-Dimethoxy-*N*,*N*-dimethyl-methanamine (62.6 mL, 471 mmol) was added to 2-amino-6-fluoro-4-(2-methoxyethoxy)benzonitrile (**11**, 52.3 mmol) at 25 °C. The resulting solution was stirred at 80 °C for 2 h, then cooled to room temperature. The mixture was poured into stirred water (200 mL) (exotherm, cold water cooling applied) and the reaction mixture stirred for 1 h. The mixture was extracted with ethyl acetate (2 × 150 mL). The combined extracts were washed with water (3 × 150 mL), saturated brine (100 mL), dried, and evaporated to dryness to afford the title compound as a white crystalline solid (13.9 g, 100%). ^{1}H NMR (500 MHz, DMSO, 27 °C) δ 2.98 (3H, s), 3.07 (3H, s), 3.29 (3H, s), 3.61−3.66 (2H, m), 4.14−4.17 (2H, m), 6.55−6.6 (2H, m), 8.03 (1H, s). m/z: ES+ [M + H]$^+$ 266.

N*-(4-{[5-Fluoro-7-(2-methoxyethoxy)quinazolin-4-yl]-amino}phenyl)-2-[4-(propan-2-yl)-1H***-1,2,3-triazol-1-yl]-acetamide (44).** A mixture of *N*-(4-aminophenyl)-2-(4-isopropyl-1*H*-1,2,3-triazol-1-yl)acetamide (**10**) (5.4 g, 20.7 mmol) and (*E*)-*N*′-(2-cyano-3-fluoro-5-(2-methoxyethoxy)phenyl)-*N*,*N*-dimethyl-formimidamide (**14**) (5.2 g, 19.7 mmol) in acetic acid (12 mL) was stirred at 60 °C for 35 min. The mixture was poured into water (150 mL), the mixture was stirred and sonicated. The resulting precipitate was collected by filtration, washed with water, and dried. The solid was dissolved in DCM/methanol (12:1, 600 mL) and the solution washed with 0.2 M NaHCO₃ solution (600 mL). The aqueous layer was

extracted with DCM/methanol (12:1, 2 × 200 mL), and the extracts were combined with the organic layer. The combined organic extracts were dried, filtered, and evaporated to give a beige solid. The crude product was crystallized from hot ethanol (700 mL). After cooling to ambient temperature and stirring for 2 h, the crystalline solid was collected by filtration, washed with cold ethanol, and dried under high vacuum at 50 °C to afford 7.4 g of crude product. The crude product was further purified by recrystallization in hot ethanol (800 mL). After cooling to ambient temperature and stirring for 20 h, the crystalline solid was collected by filtration; the solids were collected and dried under vacuum at 50 °C for 72 h to give the title compound as a white crystalline solid (6.2 g, 58%). ^{1}H NMR (500 MHz, DMSO) δ 1.27 (d, J = 6.9 Hz, 6H), 3.02 (heptd, J = 6.9, 0.6 Hz, 1H), 3.35 (s, 3H), 3.70−3.76 (m, 2H), 4.27−4.35 (m, 2H), 5.29 (s, 2H), 7.07 (d, J = 2.4 Hz, 1H), 7.15 (dd, J = 13.8, 2.4 Hz, 1H), 7.61 (d, J = 8.9 Hz, 2H), 7.69 (d, J = 8.9 Hz, 2H), 7.89 (d, J = 0.6 Hz, 1H), 8.47 (s, 1H), 8.98 (d, J = 9.7 Hz, 1H), 10.49 (s, 1H). ^{13}C NMR (125 MHz, DMSO, 27 °C) δ 22.5, 25.2, 52.1, 58.2, 68.0, 70.0, 99.8 (d, J = 11.5 Hz), 103.2 (d, J = 26.1 Hz), 104.6 (d, J = 3.2 Hz), 119.3, 122.1, 123.9, 134.3, 134.8, 152.8, 153.0, 155.6, 155.7 (d, J = 4.7 Hz), 158.5 (d, J = 253 Hz), 161.8 (d, J = 15.1 Hz), 164.2. m/z (ES+), $[M + H]^{+}$ = 480. HRMS $[MH]^{+}$ calcd for $C_{24}H_{27}N_{7}O_{3}F$: 480.2159; observed 480.2178.

ASSOCIATED CONTENT

Supporting Information

The Supporting Information is available free of charge on the ACS Publications website at DOI: 10.1021/acs.jmed-chem.8b00938.

  Protocols for the cell assays and in vivo experiments, synthetic methods for the remaining examples, and crystallographic information (PDF)

  Kinase panel selectivity data for compounds (XLSX)

  Molecular formula strings with associated data (CSV)

Accession Codes

PDB depositions are available for compounds **18** (6GQJ and 6GQO), **23** (6GQK and 6GQP), **35** (6GQL and 6GQQ), and **44** (6GQM). The authors will release the atomic coordinates and experimental data upon article publication.

AUTHOR INFORMATION

Corresponding Author

*E-mail: jason.kettle@astrazeneca.com.

ORCID

Jason G. Kettle: 0000-0001-7373-0758

Present Addresses

$^{\perp}$E.B.: H3 Biomedicine Inc., 3520, 300 Technology Square, Floor 5, Cambridge, MA 02139, U.S.

$^{\#}$S.G.: Forma Therapeutics Inc., 500 Arsenal Street, Watertown, MA 02472, U.S.

$^{\nabla}$D.O.: Peak Proteins Ltd., 3G48 Mereside, Alderley Park, Macclesfield, Cheshire, SK10 4TG, UK.

Notes

The authors declare no competing financial interest.

ACKNOWLEDGMENTS

ABBREVIATIONS USED

ADME, absorption, distribution, metabolism, excretion; ATP, adenosine triphosphate; GIST, gastrointestinal stromal tumor; PFS, progression free survival; SEM, standard error of the mean

REFERENCES

(1) Blay, J.-Y.; Casali, P. G.; Dei Tos, A. P.; Le Cesne, A.; Reichardt, P. Management of gastrointestinal stromal tumour: current practices and visions for the future. *Oncology* **2015**, *89*, 1−13.

(2) Roberts, P. J.; Eisenberg, B. Clinical presentation of gastrointestinal stromal tumors and treatment of operable disease. *Eur. J. Cancer* **2002**, *38*, S37−38.

(3) Gatta, G.; van der Zwan, J. M.; Casali, P. G.; Siesling, S.; Dei Tos, A. P.; Kunkler, I.; Otter, R.; Licitra, L.; Mallone, S.; Tavilla, A.; Trama, A.; Capocaccia, R. Rare cancers are not so rare: the rare cancer burden in Europe. *Eur. J. Cancer* **2011**, *47*, 2493−2511.

(4) Goettsch, W. G.; Bos, S. D.; Breekveldt-Postma, N.; Casparie, M.; Herings, R. M. C.; Hogendoorn, P. C. W. Incidence of gastrointestinal stromal tumours is underestimated: results of a nation-wide study. *Eur. J. Cancer* **2005**, *41*, 2868−2872.

(5) Fletcher, J. A.; Rubin, B. P. KIT mutations in GIST. *Curr. Opin. Genet. Dev.* **2007**, *17*, 3−7.

(6) Corless, C. L.; Schroeder, A.; Griffith, D.; Town, A.; McGreevey, L.; Harrell, P.; Shiraga, S.; Bainbridge, T.; Morich, J.; Heinrich, M. C. PDGFRA mutations in gastrointestinal stromal tumors: frequency, spectrum and in vitro sensitivity to imatinib. *J. Clin. Oncol.* **2005**, *23*, 5357−5364.

(7) Din, O. S.; Woll, P. J. Treatment of gastrointestinal stromal tumor: focus on imatinib mesylate. *Ther. Clin. Risk Manage.* **2008**, *4*, 149−162.

(8) Zalcberg, J.; Verweij, J.; Casali, P.; Le Cesne, A.; Reichardt, P.; Blay, J. Y.; Schlemmer, M.; Van Glabbeke, M.; Brown, M.; Judson, I. R. Outcome of patients with advanced gastro-intestinal stromal tumours crossing over to a daily imatinib dose of 800mg after progression on 400mg. *Eur. J. Cancer* **2005**, *41*, 1751−1757.

(9) Mulet-Margalef, N.; Garcia-del-Muro, X. Sunitinib in the treatment of gastrointestinal stromal tumor: patient selection and perspectives. *OncoTargets Ther.* **2016**, *9*, 7573−7582.

(10) Ferraro, D.; Zalcberg, J. Regorafenib in gastrointestinal stromal tumors: clinical evidence and place in therapy. *Ther. Adv. Med. Oncol.* **2014**, *6*, 222−228.

(11) Chen, Y.-Y.; Yeh, C.-N.; Cheng, C.-T.; Wu, C.-E.; Chiang, K.-C.; Chen, T.-W.; Wang, C.-C.; Chen, J.-S.; Yeh, T.-S. Fractioned dose regimen of sunitinib for patients with gastrointestinal stromal tumor: a pharmacokinetic and treatment efficacy study. *Transl. Oncol.* **2014**, *7*, 620−625.

(12) Grothey, A.; George, S.; van Cutsem, E.; Blay, J.-Y.; Sobrero, A.; Demetri, G. D. Optimizing treatment outcomes with regorafenib: personalized dosing and other strategies to support patient care. *Oncologist* **2014**, *19*, 669−680.

(13) Jung, F. H.; Morgentin, R. R.; Ple, P. Quinoline Derivatives. PCT Int. Appl. WO2007099323, 2007.

(14) Jung, F. H.; Ple, P. Quinazoline Derivatives. PCT Int. Appl. WO2007099317, 2007.

(15) Jung, F. H.; Ple, P. Quinoline Derivatives. PCT Int. Appl. WO2007099326, 2007.

(16) Jung, F. H.; Ple, P. Quinazoline Derivatives. PCT Int. Appl. WO2006040520, 2006.

(17) Martín, J.; Poveda, A.; Llombart-Bosch, A.; Ramos, R.; López-Guerrero, J. A.; García del Muro, J.; Maurel, J.; Calabuig, S.; Gutierrez, A.; González de Sande, J. L.; Martínez, J.; De Juan, A.; Laínez, N.; Losa, F.; Alija, V.; Escudero, P.; Casado, A.; García, P.; Blanco, R.; Buesa, J. M. Deletions affecting codons 557-558 of the c-KIT gene indicate a poor prognosis in patients with completely resected gastrointestinal stromal tumors: a study by the Spanish Group for Sarcoma Research (GEIS). *J. Clin. Oncol.* **2005**, *23*, 6190−6198.

(18) Wardelmann, E.; Losen, I.; Hans, V.; Neidt, I.; Speidel, N.; Bierhoff, E.; Heinicke, T.; Pietsch, T.; Büttner, R.; Merkelbach-Bruse, S. Deletion of Trp-557 and Lys-558 in the juxtamembrane domain of the

c-kit protooncogene is associated with metastatic behavior of gastrointestinal stromal tumors. *Int. J. Cancer* **2003**, *106*, 887−895.

(19) Guo, T.; Agaram, N. P.; Wong, G. C.; Hom, G.; D'Adamo, D.; Maki, R. G.; Schwartz, G. K.; Veach, D.; Clarkson, B. D.; Singer, S.; Dematteo, R. P.; Besmer, P.; Antonescu, C. R. Sorafenib inhibits the imatinib-resistant KIT T670I gatekeeper mutation in gastrointestinal stromal tumor. *Clin. Cancer Res.* **2007**, *13*, 4874−4881.

(20) Garner, A. P.; Gozgit, J. M.; Anjum, R.; Vodala, S.; Schrock, A.; Zhou, T.; Serrano, C.; Eilers, G.; Zhu, M.; Ketzer, J.; Wardwell, S.; Ning, Y.; Song, Y.; Kohlmann, A.; Wang, F.; Clackson, T.; Heinrich, M. C.; Fletcher, J. A.; Bauer, S.; Rivera, V. M. Ponatinib inhibits polyclonal drug-resistant KIT oncoproteins and shows therapeutic potential in heavily pretreated gastrointestinal stromal tumor (GIST) patients. *Clin. Cancer Res.* **2014**, *20*, 5745−5755.

(21) Aleksandrov, A.; Simonson, T. Molecular dynamics simulations show that conformational selection governs the binding preferences of imatinib for several tyrosine kinases. *J. Biol. Chem.* **2010**, *285*, 13807−13815.

(22) DiNitto, J. P.; Deshmukh, G. D.; Zhang, Y.; Jacques, S. L.; Coli, R.; Worrall, J. W.; Diehl, W.; English, J. M.; Wu, J. C. Function of activation loop tyrosine phosphorylation in the mechanism of c-Kit auto-activation and its implication in sunitinib resistance. *J. Biochem.* **2010**, *147*, 601−609.

(23) Rose, S. BLU-285, DCC-2618 show activity against GIST. *Cancer Discovery* **2017**, *7*, 121−122.

(24) Janku, F.; Razak, A. R. A.; Gordon, M. S.; Brooks, D. G.; Flynn, D. L.; Kaufman, M.; Pitman, J.; Smith, B. D.; Somaiah, N.; De Groot, J. F.; Chen, G.; Jennings, J.; Salah, S.; Westwood, D.; Gerstenberger, E.; Rosen, O.; George, S. Pharmacokinetic-driven phase I study of DCC-2618 a pan-KIT and PDGFR inhibitor in patients (pts) with gastrointestinal stromal tumor (GIST) and other solid tumors. *J. Clin. Oncol.* **2017**, *35*, 2515.

(25) Evans, E.; Gardino, A.; Hodous, B.; Davis, A.; Zhu, J.; Kohl, N. E.; Lengauer, C. Blu-285, a potent and selective inhibitor for hematologic malignancies with KIT exon 17 mutations. *Blood* **2015**, *126*, 568.

(26) Plé, P. A.; Jung, F.; Ashton, S.; Hennequin, L.; Laine, R.; Morgentin, R.; Pasquet, G.; Taylor, S. Discovery of AZD2932, a new quinazoline ether inhibitor with high affinity for VEGFR-2 and PDGFR tyrosine kinases. *Bioorg. Med. Chem. Lett.* **2012**, *22*, 262−266.

(27) Plé, P. A.; Jung, F.; Ashton, S.; Hennequin, L.; Laine, R.; Lambert-van der Brempt, C.; Morgentin, R.; Pasquet, G.; Taylor, S. Discovery of new quinoline ether inhibitors with high affinity and selectivity for PDGFR tyrosine kinases. *Bioorg. Med. Chem. Lett.* **2012**, *22*, 3050−3055.

(28) Goldberg, F. W.; Kettle, J. G.; Kogej, T.; Perry, M. W. D.; Tomkinson, N. P. Designing novel building blocks is an overlooked strategy to improve compound quality. *Drug Discovery Today* **2015**, *20*, 11−17.

(29) Beglov, D.; Roux, B. An integral equation to describe the solvation of polar molecules in liquid water. *J. Phys. Chem. B* **1997**, *101*, 7821−7826.

(30) Kettle, J. G.; Wilson, D. M. Standing on the shoulders of giants: a retrospective analysis of kinase drug discovery at AstraZeneca. *Drug Discovery Today* **2016**, *21*, 1596−1608.

(31) Bergenholm, L.; Parkinson, J.; Mettetal, J.; Evans, N. D.; Chappell, M. J.; Collins, T. Predicting QRS and PR interval prolongations in humans using nonclinical data. *Br. J. Pharmacol.* **2017**, *174*, 3268−3283.